SCIENCE CHINA Materials ARTICLES

mater.scichina.com link.springer.com

Published online 30 June 2021 | https://doi.org/10.1007/s40843-021-1696-x
Sci China Mater 2021, 64(12): 2997–3006

Synergistically electronic tuning of metalloid CdSe nanorods for enhanced electrochemical CO_2 reduction

Tao Chen[1,2], Tianyang Liu[3], Xinyi Shen[1], Wei Zhang[1], Tao Ding[1], Lan Wang[1,2], Xiaokang Liu[1], Linlin Cao[1], Wenkun Zhu[2*], Yafei Li[3*] and Tao Yao[1*]

ABSTRACT **Engineering the electronic properties of catalysts to target intermediate adsorption energy as well as harvest high selectivity represents a promising strategy to design advanced electrocatalysts for efficient CO_2 electroreduction. Herein, a synergistical tuning on the electronic structure of the CdSe nanorods is proposed for boosting electrochemical reduction of CO_2. The synergy of Ag doping coupled with Se vacancies tuned the electronic structure of the CdSe nanorods, which shows the metalloid characterization and thereby the accelerated electron transfer of CO_2 electroreduction. *Operando* synchrotron radiation Fourier transform infrared spectroscopy and theoretical simulation revealed that the Ag doping and Se vacancies accelerated the CO_2 activation process and lowered the energy barrier for the conversion from CO_2 to *COOH; as a result, the performance of CO_2 electroreduction was enhanced. The as-obtained metalloid Ag-doped CdSe nanorods exhibited a 2.7-fold increment in current density and 1.9-fold Faradaic efficiency of CO compared with the pristine CdSe nanorod.**

Keywords: cadmium selenium, Ag doping, Se vacancies, CO_2 electroreduction

INTRODUCTION

Electrochemical reduction of carbon dioxide (CO_2) into value-added chemicals by abundant renewable energy sources (such as wind and solar energy) and water has been identified as a prospective strategy for simultaneously satisfying renewable energy storage and a closed carbon cycle [1–6]. The pivotal bottleneck lies in the activation of CO_2 into the radical anion, which requires a relatively high reduction potential during CO_2 reduction reaction (CO_2RR) [7–9]. Electron transferring to CO_2 molecules is usually regarded as a critical step in the process of CO_2 activation [10–16]. To overcome this bottleneck, efficient and robust electrocatalysts with electron donor centers to trap CO_2 molecules and activate stable C=O nonpolar bonds should be explored, which is essential for the development of future renewable energy sources and implementation of CO_2 mitigation systems.

The earth-abundant cadmium-based catalysts have been employed as star materials for CO_2 electroreduction to CO. For example, lamellar inorganic-organic hybrid $Zn_xCd_{1-x}S$-amine was designed through the combination of amine incorporation and partial heteroatom substitution for efficiently synthesizing syngas with tunable CO/H_2 ratios [17]. However, the electrocatalytic performance of most cadmium-based catalysts is still limited by the high potential required for CO_2 activation. As well known, the CO_2 activation involves the transfer of electrons from the catalyst to the CO_2 molecules, which is closely related to the local electronic structure of the catalyst [18–21]. One effective strategy to regulate the local electronic structure of electrocatalysts is elemental doping, considering that the introduction of heteroatoms causes energy level hybridization between the original catalysts and dopants [22–25]. Previous research confirmed that heteroatom doping was capable of manipulating the d-band center, band structure, charge distribution and valence state of the active site, and thereby electrochemical activity was enhanced [26–29]. For instance, a defect level was introduced by ultrathin SnS_2 nanosheets with the Ni dopants, leading to the decreased work function, and thereby the CO_2 activation

[1] National Synchrotron Radiation Laboratory, University of Science and Technology of China, Hefei 230029, China
[2] State Key Laboratory of Environmentally Friendly Energy Materials, School of National Defense Science and Technology, Southwest University of Science and Technology, Mianyang 621010, China
[3] Jiangsu Collaborative Innovation Centre of Biomedical Functional Materials, Jiangsu Key Laboratory of New Power Batteries, School of Chemistry and Materials Science, Nanjing Normal University, Nanjing 210023, China
* Corresponding authors (emails: zhuwenkun@swust.edu.cn (Zhu W); liyafei@njnu.edu.cn (Li Y); yaot@ustc.edu.cn (Yao T))

was accelerated [30]. Parallel to the elemental doping, the facilitation of CO_2 activation commonly originates from the tailored active sites through engineering the coordination environment of catalysts, which can be achieved simply by introducing vacancies [31–33]. For example, the rich S vacancies in CdS-carbon nanotubes (CNTs) have been confirmed to effectively decrease the overpotential for CO_2 activation, so as to significantly accelerate the process of CO_2 activation and promote the conversion of COOH* to CO* [6]. Therefore, the integration of element doping and vacancies provides a potential strategy to improve CO_2 activation by engineering the electronic structure of electrocatalysts, and thereby CO_2 electroreduction can be enhanced.

Herein, we report synergistical tuning on the electronic structure of the metalloid CdSe nanorods *via* Ag doping and Se vacancies to boost the electrochemical reduction of CO_2. The Ag-doped CdSe nanorods with Se vacancies exhibited a higher current density and Faradaic efficiency (FE) for CO, compared with the pristine CdSe nanorods. When the Ag content was 3.1 atm%, the Ag-doped CdSe nanorods with Se vacancies exhibited a considerable FE of 91% for CO with the current density of 19.68 mA cm^{-2} at −1.15 V *vs.* reversible hydrogen electrode (RHE). Under the potentiostatic examination, the Ag-doped CdSe nanorods preserved a steady FE for CO without drastic decay of current density. *Operando* synchrotron radiation Fourier transform infrared spectroscopy (SR-FTIR) and theoretical calculations results further confirmed that the local electronic structure of the electrocatalyst surface was affected by the integration of Ag doping and Se vacancies, which decreased the energy barrier for the conversion of CO_2 to *COOH, resulting in dramatically improved performance for the electrochemical reduction of CO_2.

EXPERIMENTAL SECTION

The experimental details are provided in the Supplementary information. This section briefly summarizes the synthesis procedures.

Preparation of CdSe nanorods

CdSe nanorods were prepared by a simple amine-assisted solvothermal method. Firstly, 2 mmol of $CdCl_2{\cdot}2.5H_2O$ was dissolved in 60 mL of ethylenediamine (EDA) under vigorous stirring, and a homogeneous solution was formed. Next, 2 mmol of Se powder was added into the above solution followed by the injection of 6 mL of N_2H_4. After being stirred for 30 min, the mixture was transferred into a 100-mL Teflon-lined stainless steel autoclave, maintained at 140°C for 12 h. The product was centrifuged when the reaction was completed. The products were washed using deionized water (DIW) thrice and ethanol twice, and then dried at 60°C for 24 h.

Preparation of Ag-doped CdSe nanorods

In a standard cation exchange reaction, pristine CdSe nanorods (20 mg) were dispersed into DIW, followed by the addition of 1 mL of an aqueous solution containing various amounts of $AgNO_3$ (0.4, 0.8, and 1.2 mg), respectively. The mixture was transferred into a 25-mL Teflon-lined stainless steel autoclave after being stirred for 30 min, maintained at 160°C for 6 h. The Ag-doped CdSe nanorods were obtained after being washed thrice with the mixture of ethanol and DIW.

RESULTS AND DISCUSSION

Preparation and characterization of Ag-doped CdSe nanorods

The synthesis of Ag-doped CdSe nanorods is schematically illustrated in Fig. 1a. Firstly, the pristine CdSe nanorods were synthesized by a simple amine-assisted solvothermal method according to the previous reports [34,35]. Next, Ag-doped CdSe nanorods with different doping levels were prepared by ion exchange. Determined by the inductively coupled plasma atomic emission spectroscopy (ICP-AES), the mass ratios of Ag/Ag-doped CdSe were 0.9%, 1.9%, and 3.1%. As such, the Ag-doped CdSe nanorods with different doping levels were termed as 0.9% Ag-CdSe, 1.9% Ag-CdSe, and 3.1% Ag-CdSe nanorods, respectively. As depicted in Fig. 1b, and Figs S1, S2, all Ag-doped samples presented the nanorod morphology. To further visualize the crystalline structure of the Ag-doped CdSe nanorods, the high-angle annular dark field scanning transmission electron microscopy (HAADF-STEM) was measured as shown in Fig. 1c. The HAADF-STEM image shows that homogeneously doped Ag-CdSe nanorods were highly crystalline with wurtzite structure. The typical lattice fringe with lattice spacing of 0.34 nm corresponded to the (002) plane of wurtzite CdSe [36]. The Ag-doped CdSe nanorods revealed negligible variations in the lattice spacing compared with CdSe nanorods, implying that the basic crystal structure was well preserved upon the ion exchange process (Fig. S3). The energy dispersive X-ray (EDX) elemental mapping and spectra of 3.1% Ag-CdSe nanorods shown in Fig. 1d and Fig. S4 demonstrate homogeneous distribution of Ag, Se and Cd in the entire sample. Moreover, all Ag-doped CdSe nanorods presented similar diffraction peaks to those of wurtzite CdSe as shown in X-ray diffraction

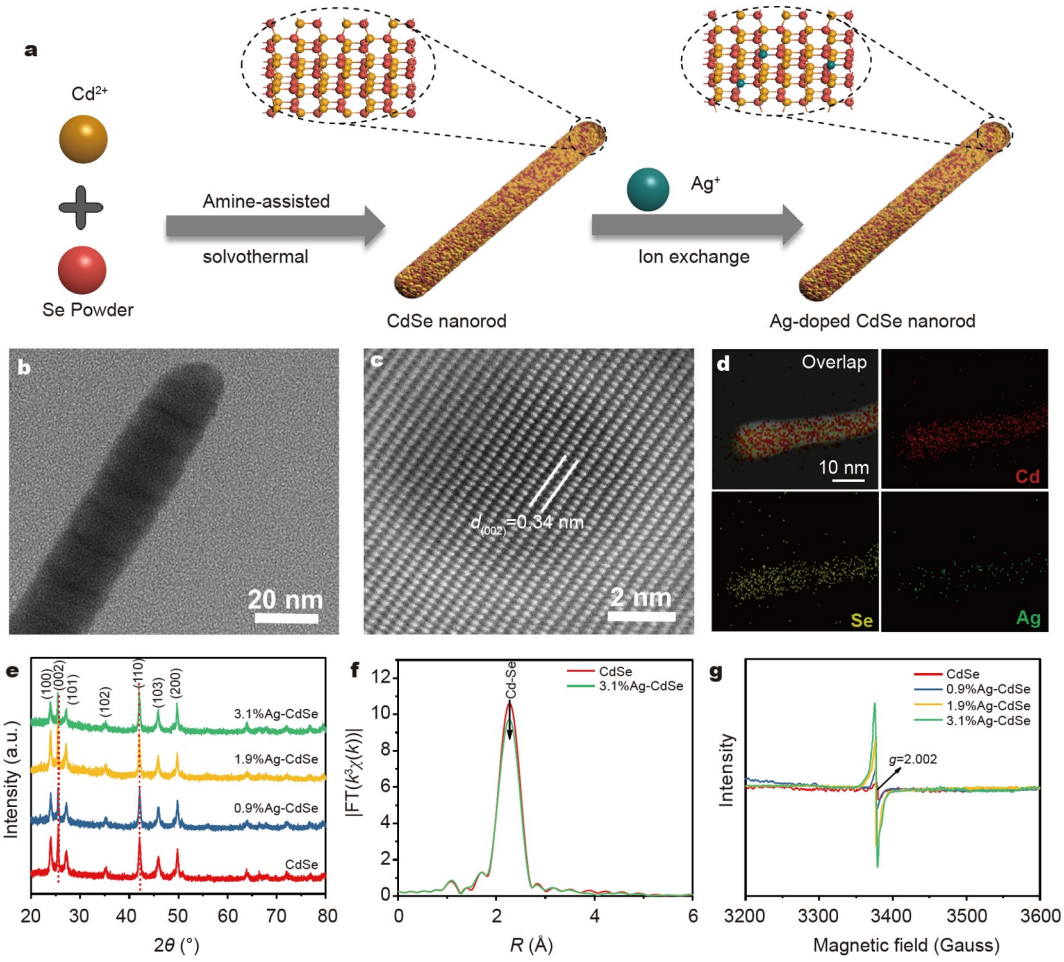

Figure 1 (a) Schematic illustration of the manufacture of the Ag-doped CdSe nanorods. (b) TEM and (c) high-resolution TEM images of the 3.1% Ag-CdSe nanorods. (d) HAADF-STEM and STEM-EDX elemental mapping images of an individual 3.1% Ag-CdSe nanorod. (e) XRD patterns of the pristine CdSe and Ag-doped CdSe nanorods. (f) The FT of the EXAFS for the pristine CdSe and 3.1% Ag-CdSe nanorods. (g) ESR spectra of the pristine CdSe and Ag-doped CdSe nanorods.

(XRD) patterns (Fig. 1e), and no Ag-related phases appeared [37]. The Ag 3d X-ray photoelectron spectroscopy (XPS) spectra of Ag-doped CdSe exhibited two typical peaks located at 373.7 and 367.8 eV, which were attributed to Ag $3d_{3/2}$ and Ag $3d_{5/2}$ (Figs S5, S6), respectively, indicating that monovalent Ag^{+} presumably occupied the substitution site of bivalent Cd^{2+} inside CdSe. The Cd 3d and Se 3d XPS peaks both shifted slightly to the low-*E* region with the increasing amount of Ag doping, resulting from the electron transfer (Figs S7, S8).

Considering that vacancies are usually generated when the high-valence cations in the transition metal dichalcogenide (TMD) are replaced by low-valence cations due to the charge conservation. Synchrotron radiation X-ray absorption fine structure (XAFS) measurements were employed at Cd K-edge, Se K-edge and Ag K-edge of pristine CdSe and 3.1% Ag-CdSe nanorods, respectively, to investigate the influence of Ag doping on local atomic arrangements and electronic structures of CdSe nanorods. As shown in Fig. S9, the overall Cd K-edge X-ray absorption near-edge structure (XANES) spectral shape for the Ag-doped CdSe is almost close to that of CdSe, except for the low-*E* shift of the white-line peak, which may be attributed to the decrease in the valence of Cd from the Ag doping [38]. Furthermore, the Fourier transform (FT) of the extended XAFS (EXAFS) curve for pristine CdSe and 3.1% Ag-CdSe nanorods shows a main peak at 2.26 Å corresponding to the Cd-Se coordination (Fig. 1f). However, intensity of FT peak decreases slightly for the 3.1% Ag-CdSe nanorods, in relation to that of pristine CdSe. The quantitative EXAFS curve fitting analysis demonstrated that the coordination number of

Cd-Se for 3.1% Ag-CdSe is 3.6, smaller than that for the pristine CdSe (4.0), which further confirmed the substitutional doping of monovalent Ag^+ for bivalent Cd^{2+} in CdSe (Table S1 and Fig. S10). Similarly, the EXAFS curve of 3.1% Ag-CdSe is close to that of the pristine CdSe except the slight decline of Se-Cd coordination peak at 2.45 Å (Fig. S11). The Se-Cd coordination number of 3.1% Ag-CdSe nanorods (3.4) is lower than 4.0, that for the pristine CdSe nanorods (Table S1 and Fig. S12). The decreased Se-Cd coordination number may be ascribed to the generation of Se vacancies induced by Ag doping. The Ag K-edge XANES spectrum for 3.1% Ag-CdSe is obviously different from that of Ag foil (Fig. S13a). The Ag K-edge FT curve for 3.1% Ag-CdSe shows one dominant peak at 2.46 Å, which is assigned to the Ag-Se coordination (Figs S13b, S14), further confirming the substitutional doping of Ag^+. Electron spin resonance (ESR) measurements were further performed to verify the existence of the Se vacancies in the Ag-doped CdSe nanorods. As exhibited in Fig. 1g, the pristine CdSe nanorods exhibited a weak ESR resonance, demonstrating a low concentration of native Se vacancies [39]. The signal of Se vacancies at the g value of 2.002 was significantly enhanced upon the introduction of Ag^+ cations, which further proved the generation of new Se vacancies. Combining the XAFS and ESR results, it is believed that the substitution of monovalent Ag^+ for divalent Cd^{2+} was accompanied by the generation of Se vacancies in the CdSe nanorods.

Electrocatalytic CO_2RR performances of Ag-doped CdSe nanorods

Element doping-induced Se vacancies offers a potential prospect to enhance the electrochemical reduction of CO_2. The electrocatalytic CO_2RR performance of the pristine CdSe and Ag-doped CdSe nanorods could be probed in a H-cell containing 70 mL of 0.1 mol L^{-1} $KHCO_3$. Fig. S15 shows the linear sweep voltammetry (LSV) curves of the pristine CdSe and Ag-doped CdSe nanorods under CO_2 and Ar. The Ag-doped CdSe nanorods demonstrated higher geometrical current density under CO_2 relative to that under Ar, indicating the higher electrocatalytic activity toward CO_2 electroreduction. Especially, the geometrical current density of the 3.1% Ag-CdSe nanorods was 19.68 mA cm^{-2} under the overpotential of −1.15 V *vs.* RHE, which was 2.7 times higher than that of the original CdSe nanorods (Fig. 2a). In the CdSe-based electrocatalytic CO_2RR system, CO was the only carbonaceous product indicated by gas chromatography (GC) and ^{1}H nuclear magnetic resonance (^{1}H NMR). Fig. 2b displays the partial current densities for CO production (j_{CO}) of the pristine CdSe and Ag-doped CdSe nanorods. Specifically, the 3.1% Ag-CdSe nanorods exhibited a considerable partial current density of 14.9 mA cm^{-2} for CO at −1.15 V *vs.* RHE. Fig. 2c shows the FE of the four CdSe-based electrocatalysts for CO production under applied overpotentials. Notably, the 3.1% Ag-CdSe nanorods displayed the highest FE of 91% for CO production at the overpotential of −1.15 V *vs.* RHE, which was 1.9 times that on the pristine CdSe nanorods (48.2% at −1.15 V *vs.* RHE). To further study the influence of doping amount on the electrocatalytic CO_2 reduction performance of CdSe nanorods, the CdSe nanorods with higher Ag doping amounts were considered. Under the condition of 4.8 atm% Ag content, the 4.8% Ag-CdSe nanorods exhibited a relative FE of 72% for CO with the current density of 22.44 mA cm^{-2} at −1.15 V *vs.* RHE (Fig. S16). The decreased FE for CO presumably resulted from the fact that part of the Ag as nanoparticles was loaded on the CdSe nanorods. The above results can be further confirmed by TEM images of 4.8% Ag-CdSe nanorods (Fig. S17). To confirm that the Ag doping and Se vacancies synergistically enhance CO_2 electrochemical reduction, the performance of CO_2 conversion in the CdSe nanorods with Se vacancies ($CdSe_{1-x}$) was compared. As expected, the $CdSe_{1-x}$ nanorods displayed a lower FE for CO relative to the Ag-doped CdSe nanorods (Fig. S18). Therefore, the above results suggested that the integration of Ag doping and Se vacancies in the CdSe nanorods synergistically enhanced the selectivity to CO. Notably, as shown in Table S2, the Ag-doped CdSe nanorods exhibited a considerable j_{CO} of 19.68 mA cm^{-2} with FE of 91%, outperforming most related electrocatalysts for CO production [6,17,40–45]. In addition, the durability of the pristine CdSe and 3.1% Ag-CdSe nanorods for CO_2 electroreduction to CO was examined by current-time (I-t) measurements at the potentiostatic of −1.15 V *vs.* RHE (Fig. 2d and Fig. S19). The pristine CdSe and 3.1% Ag-CdSe nanorods presented decay of less than 5% in current density with relative stable FE for CO production after a 10-h potentiostatic characterization. Accordingly, we further characterized the morphology and crystal structure of the 3.1% Ag-CdSe nanorods after a 10-h electrocatalytic reaction. The results demonstrated almost no change in the morphology and crystal structure of the 3.1% Ag-CdSe nanorods after the reaction (Fig. S20). The stability test indicated that the Ag-doped CdSe nanorods served as prospective electrocatalysts to continuously produce CO with a remarkable current density during the CO_2 electroreduction.

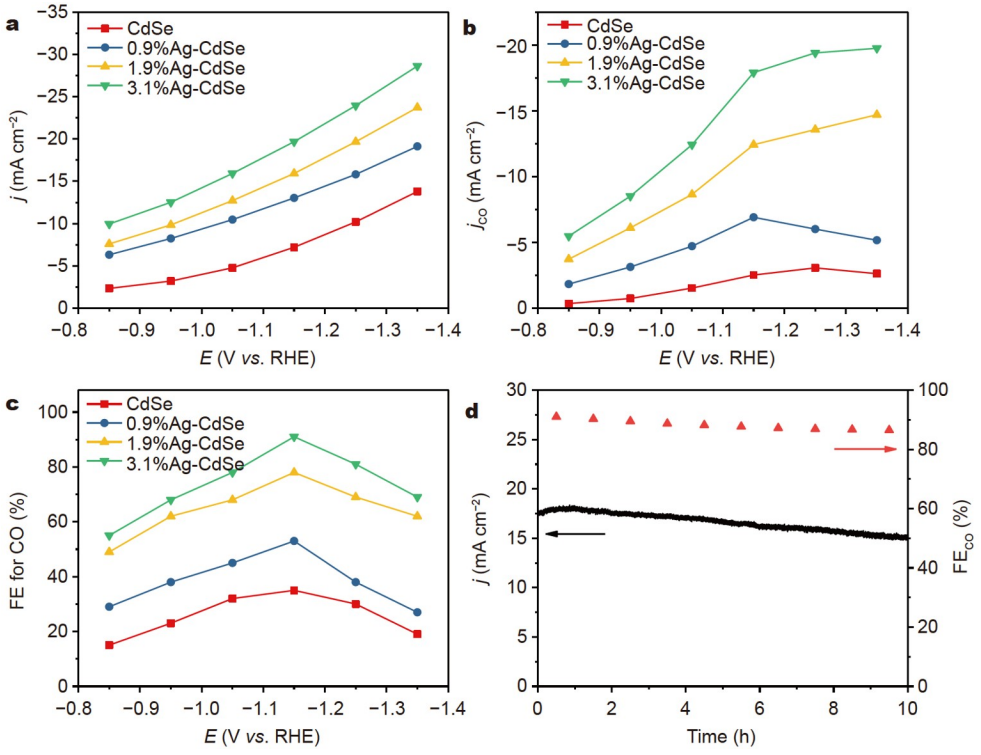

Figure 2 (a) Geometrical current densities (*j*), (b) partial current densities for CO production (j_{CO}) and (c) Faradaic efficiencies for CO production (FE_{CO}) over the pristine CdSe and Ag-doped CdSe nanorods. (d) Plot of geometrical current densities (*j*) and FE_{CO} *versus* time over the 3.1% Ag-CdSe nanorods at a constant potential of −1.15 V*vs.* RHE.

Theoretical investigation

The significant improvement of CO_2 electrochemical reduction performance inspired us to in-depth investigate the intrinsic activity and related microkinetics. As shown in Figs S21, S22, the double-layer capacitance (C_{dl}) values increased slightly from 5.75 mF cm^{-2} of the original CdSe nanorods to 6.04 mF cm^{-2} of the 3.1% Ag-CdSe nanorods. According to the C_{dl} value, the normalized j_{CO} for the 3.1% Ag-CdSe nanorods was 6.8-folder higher than that of the pristine CdSe nanorods at −1.15 V *vs.* RHE, indicating that the Ag-doped induced Se vacancies synergistically promoted the intrinsic activity of active sites (Fig. S23). As exhibited in Fig. 3a, the Tafel slopes of the original CdSe and 3.1% Ag-CdSe nanorods were determined to be 139.8 and 108.5 mV dec^{-1} respectively, demonstrating the rate-determining step for the activation process of CO_2 [46]. The *IR*-compensated oxidative LSV scans in 0.1 moL L^{-1} KOH electrolyte for OH^- adsorption was applied to verify the binding strength of CO_2 (Fig. 3b) [47]. The pristine CdSe nanorods presented a single oxidation peak at 0.185 V *vs.* RHE, indicating the OH^- adsorption on the original active sites. For the 3.1% Ag-CdSe nanorods, the oxidation peak shifted negatively to 0.177 V due to the decreased overpotential by the conductivity improvement in the catalysts. Furthermore, a satellite peak at 0.138 V appeared in the 3.1% Ag-CdSe nanorods, demonstrating the formation of strong adsorption sites. To further verify that the Ag doping-induced formation of Se vacancies effectively enhanced the chemical adsorption of CO_2, the CO_2 adsorption isotherms of the pristine CdSe, $CdSe_{1-x}$ and 3.1% Ag-CdSe nanorods were performed, as shown in Fig. S24. In CO_2 adsorption isotherms, the 3.1% Ag-CdSe and $CdSe_{1-x}$ nanorods possessed the CO_2 adsorption capacity of 171.3 and 195.2 mmol g^{-1} at 1 atm (1 atm = 101.3 kPa), respectively, which were 1.8 times and 2.1 times that of the pristine CdSe nanorods. Therefore, the CO_2 chemical adsorption on CdSe nanorods was enhanced by the formation of Se vacancies through Ag doping, thus significantly contributing to the process of CO_2 activation. The facilitated electron-transfer process was confirmed by the Nyquist plots of the original CdSe and Ag-doped CdSe nanorods (Fig. 3c). The 3.1% Ag-CdSe nanorods displayed the charge-transfer resistance (R_{CT}) of 9.5 Ω, which was lower compared with that (20.2 Ω) of original CdSe nanorods. Furthermore, Mott-schottky plots display

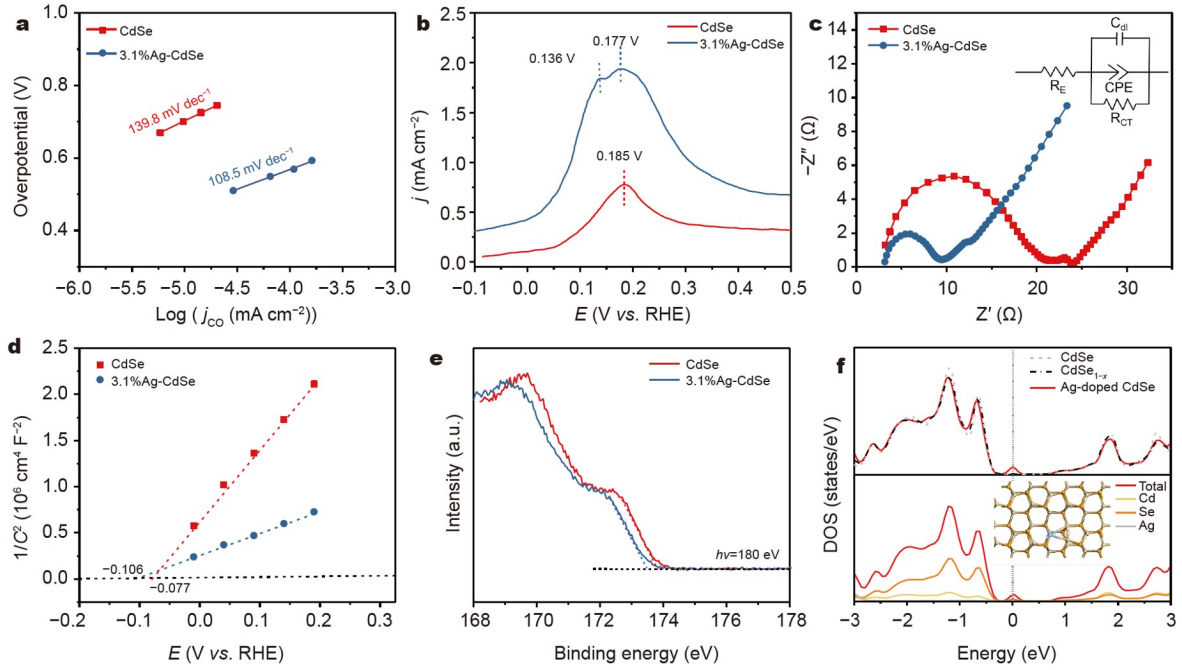

Figure 3 (a) Tafel plots, (b) single oxidative LSV scans plots, (c) Nyquist plots, (d) Mott-Schottky plots and (e) secondary electron cutoff of the UPS spectra for the pristine CdSe and 3.1% Ag-CdSe nanorods. (f) Calculated DOS of the CdSe, $CdSe_{1-x}$ and Ag-doped CdSe slabs.

that the slope (dC^{-2}/dV) of original CdSe nanorods was 3.3-fold higher than that of 3.1% Ag-CdSe nanorods, demonstrating the carrier density (N_D) of the 3.1% Ag-CdSe nanorods was 3.3 times higher than the original CdSe nanorods. (Fig. 3d). The secondary electron cutoff of the ultraviolet photoelectron spectroscopy (UPS) spectra shown in Fig. 3e indicated the work function of the pristine CdSe nanorods was decreased by 0.5 eV after the incorporation of Ag, which was ascribed to the increase in N_D. Taken together, the Ag doping and Se vacancies synergistically accelerated the CO_2 activation process, thus leading to the accelerated charge transfer process of CO_2 reduction.

In order to reveal the essence of the dramatic difference in CO_2 reduction kinetics, the electronic structures of the original CdSe and Ag-doped CdSe nanorods were explored in terms of theory. The calculated density of states (DOS) of the CdSe, $CdSe_{1-x}$, and Ag-doped CdSe slabs were performed using density functional theory (DFT) methods (Fig. 3f). The Ag-doped CdSe displayed an obvious DOS peak at the Fermi level compared with the original CdSe. The distinct DOS peak appearing at the Fermi level indicated that the Ag-doped CdSe possessed metalloid conductive nature, which further proved that the integration of Ag doping and Se vacancies enhanced the conductivity of the material itself [48]. Taking the photonic DOS contribution of each element into account, the appearance of the peak at the Fermi level originates from the electronic structure of the CdSe slabs harmonized by Ag doping, instead of the contribution of the impurity level by Ag doping.

Operando synchrotron radiation SR-FTIR for electrocatalysis was then performed to gain insight into the underlying CO_2RR mechanism over the Ag-doped CdSe nanorods (Fig. 4a). *Operando* SR-FTIR spectra were recorded at −0.55, −0.75, −0.95, and −1.15 V under CO_2 flowing in the electrocatalytic reaction system. As shown in Fig. 4b, the typical peaks appearing at ~1520, ~1540, ~1660 and ~1694 cm^{-1} continually increased as cathodic potentials lapsed. The monodentate carbonate groups (m-CO_3^{2-}) appeared at the peak of ~1520 cm^{-1}, indicating that the m-CO_3^{2-} adsorbed on the electrocatalyst surface rose as the applied voltage decreased. Considering that the peak at ~1695 cm^{-1} is attributed to the adsorption of $CO_2^{\cdot-}$ radicals on the catalyst surface, more CO_2 molecules were activated during the reaction. The peak at ~1660 cm^{-1} resulting from the *COOH was the key intermediates for CO_2 electroreduction. Based on the intermediates detected by *operando* SR-FTIR spectra, the electrochemical reaction pathway of CO_2 to CO over the Ag-doped CdSe nanorods was further proposed (Fig. 4c). Typically, the electrons from the electrode could be

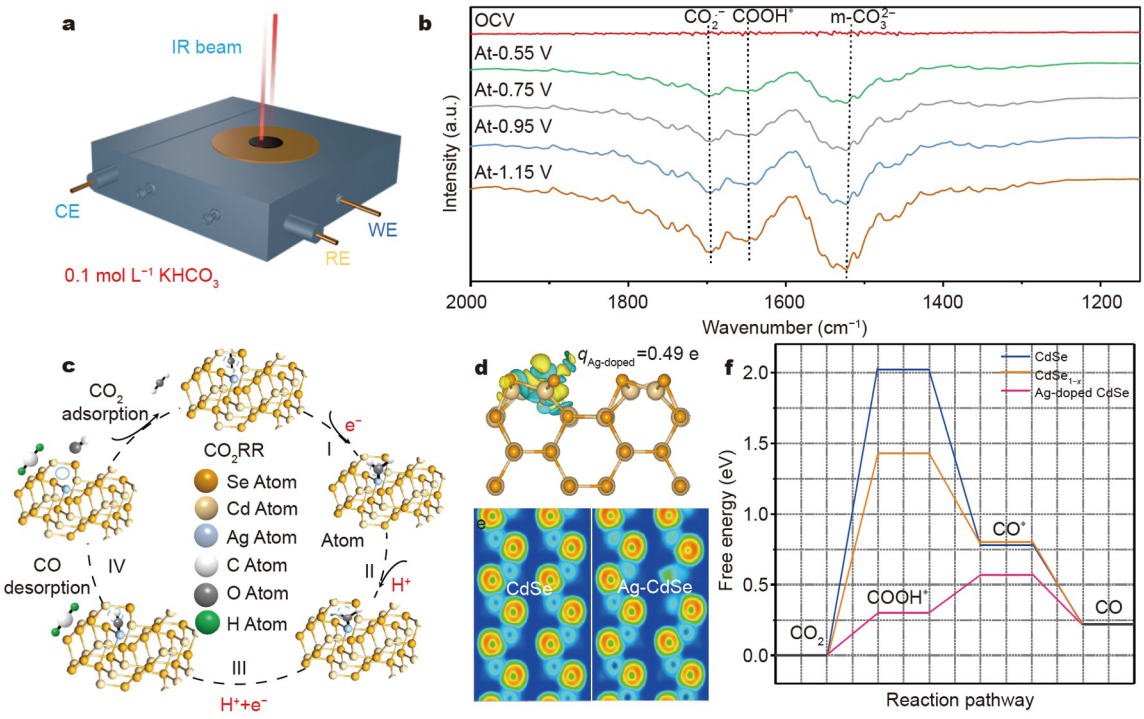

Figure 4 (a) Schematic of the *operando* SR-FTIR set-up. (b) *Operando* SR-FTIR of the Ag-doped CdSe nanorods under the working condition. (c) Schematic of the whole CO_2RR mechanism on the Ag-doped CdSe nanorods. (d) Electron density difference plot of the *COOH intermediate adsorption structure for Ag-doped CdSe. Yellow contours indicate electron accumulation and light green contours denote electron deletion. (e) ELF for CdSe and Ag-doped CdSe (110). The blue and red areas represnt low and high electron localization, respectively. (f) Gibbs free energy diagrams for CO_2 reduction to CO on CdSe, $CdSe_{1-x}$, and Ag-doped CdSe slabs. The * represents an adsorption site. OCV: open circuit voltage; WE: working electrode; RE: reference electrode; CE: counter electrode.

transformed on CO_2 molecules captured by the Se vacancies in the Ag-doped CdSe, which was further activated to form the *COOH intermediate by $1H^+/1e^-$ transfer (Equation (1)). Next, the proton-coupled electron transfers for the formation of *CO intermediate with the desorption of a water molecule (Equation (2)) [49]. Finally, the CO molecule was desorbed from the surface of the Ag-doped CdSe for the final CO product (Equation (3)).

Step 1:

$$CO_2(g) + H^+(aq) + e^- + * \rightarrow *COOH \text{ (activation process)}; \quad (1)$$

Step 2:

$$*COOH + H^+(aq) + e^- \rightarrow *CO + H_2O(l) \text{ (surface reaction)}; \quad (2)$$

Step 3:

$$CO* \rightarrow CO(g) + * \text{ (desorption process)}. \quad (3)$$

To reveal the CO_2 activation process on the original CdSe and Ag-doped CdSe nanorods, the electronic interaction between the electrocatalysts and adsorbate was analyzed by DFT calculations. Considering that the final product of the CO_2 reduction on the original CdSe and Ag-doped CdSe nanorods is CO, we focused on the pathway for CO product from the *COOH intermediate. According to structural optimization, *COOH intermediates tended to form bridge bonds with the two different metal atoms of both the original CdSe and Ag-doped CdSe slabs (Fig. 4d and Fig. S25). The adsorption of *COOH on the Ag-CdSe surface requires more electrons than that on the surface of CdSe, indicating that the adsorption strength of *COOH on CdSe can be enhanced by Ag doping [50]. The electronic localization functions (ELF) revealed the electron density around Ag was significantly reduced upon Ag doping induced Se vacancies (Fig. 4e). The results indicate that the presence of Ag harmonizes the electronic structure of the entire system, promoting the electroreduction of CO_2 to CO. Furthermore, the Gibbs free energy of CO_2 reduction to CO over CdSe, $CdSe_{1-x}$ and Ag-CdSe was calculated by DFT stimulations. As shown in Fig. 4f, for CdSe, $CdSe_{1-x}$, and

Ag-CdSe, the formation of *COOH is further confirmed to be the rate-limiting step for CO_2RR, which is consistent with the results of Tafel slopes. The Se vacancies induced by the Ag doping greatly decreased the barrier for the formation of *COOH compared with pristine CdSe, thus enhancing the subsequent reduction process, and ultimately the CO production activity was enhanced. Especially, our calculations are in good accordance with the experimental resistance measurements.

CONCLUSIONS

In conclusion, we developed metalloid Ag-doped CdSe nanorods as efficient catalysts for the electrochemical transformation from CO_2 to CO. The substitution of divalent Cd^{2+} with monovalent Ag^+ is accompanied by the *in situ* generation of Se vacancies. The Ag doping-induced Se vacancies in CdSe nanorods synergistically contributed to both FE for CO and current density. Specifically, at −1.15 V *vs.* RHE, the Ag-doped CdSe nanorods showed a considerable FE of 91% for CO with the current density of 19.68 mA cm^{-2}. *Operando* SR-FTIR and theoretical calculations revealed that the Ag doping coupled with Se vacancies manipulated the electronic structure of the electrocatalyst surface and lowered the energy barrier for the conversion of CO_2 to *COOH intermediate. This work may provide a span-new path for the design of promising catalysts for CO_2 electroreduction.

Received 5 March 2021; accepted 27 April 2021; published online 30 June 2021

1 Liu Y, Tian D, Biswas AN, *et al.* Transition metal nitrides as promising catalyst supports for tuning CO/H_2 syngas production from electrochemical CO_2 reduction. Angew Chem Int Ed, 2020, 59: 11345–11348
2 Zhang W, Huang C, Xiao Q, *et al.* Atypical oxygen-bearing copper boosts ethylene selectivity toward electrocatalytic CO_2 reduction. J Am Chem Soc, 2020, 142: 11417–11427
3 Shen X, Liu X, Wang S, *et al.* Synergistic modulation at atomically dispersed Fe/Au interface for selective CO_2 electroreduction. Nano Lett, 2021, 21: 686–692
4 Daiyan R, Tan X, Chen R, *et al.* Electroreduction of CO_2 to CO on a mesoporous carbon catalyst with progressively removed nitrogen moieties. ACS Energy Lett, 2018, 3: 2292–2298
5 Wu J, Xie Y, Du S, *et al.* Heterophase engineering of SnO_2/Sn_3O_4 drives enhanced carbon dioxide electrocatalytic reduction to formic acid. Sci China Mater, 2020, 63: 2314–2324
6 Qin B, Li Y, Wang H, *et al.* Efficient electrochemical reduction of CO_2 into CO promoted by sulfur vacancies. Nano Energy, 2019, 60: 43–51
7 He Y, Li Y, Zhang J, *et al.* Low-temperature strategy toward Ni-NC@Ni core-shell nanostructure with single-Ni sites for efficient CO_2 electroreduction. Nano Energy, 2020, 77: 105010
8 Li X, Xi S, Sun L, *et al.* Isolated FeN_4 sites for efficient electrocatalytic CO_2 reduction. Adv Sci, 2020, 7: 2001545
9 Wang T, Sang X, Zheng W, *et al.* Gas diffusion strategy for inserting atomic iron sites into graphitized carbon supports for unusually high-efficient CO_2 electroreduction and high-performance Zn-CO_2 batteries. Adv Mater, 2020, 32: 2002430
10 Cheng H, Liu S, Zhang J, *et al.* Surface nitrogen-injection engineering for high formation rate of CO_2 reduction to formate. Nano Lett, 2020, 20: 6097–6103
11 Tao Z, Wu Z, Wu Y, *et al.* Activating copper for electrocatalytic CO_2 reduction to formate *via* molecular interactions. ACS Catal, 2020, 10: 9271–9275
12 Geng Z, Cao Y, Chen W, *et al.* Regulating the coordination environment of Co single atoms for achieving efficient electrocatalytic activity in CO_2 reduction. Appl Catal B-Environ, 2019, 240: 234–240
13 Kong X, Liu Y, Li P, *et al.* Coordinate activation in heterogeneous carbon dioxide reduction on Co-based molecular catalysts. Appl Catal B-Environ, 2020, 268: 118452
14 Shang H, Wang T, Pei J, *et al.* Design of a single-atom indium$^{\delta+}$–N_4 interface for efficient electroreduction of CO_2 to formate. Angew Chem Int Ed, 2020, 59: 22465–22469
15 Zhang N, Zhang X, Tao L, *et al.* Silver single-atom catalyst for efficient electrochemical CO_2 reduction synthesized from thermal transformation and surface reconstruction. Angew Chem Int Ed, 2021, 60: 6170–6176
16 Jiang Z, Wang T, Pei J, *et al.* Discovery of main group single Sb–N_4 active sites for CO_2 electroreduction to formate with high efficiency. Energy Environ Sci, 2020, 13: 2856–2863
17 Meng N, Liu C, Liu Y, *et al.* Efficient electrosynthesis of syngas with tunable CO/H_2 ratios over $Zn_xCd_{1-x}S$-amine inorganic-organic hybrids. Angew Chem Int Ed, 2019, 58: 18908–18912
18 Zhang W, He P, Wang C, *et al.* *Operando* evidence of Cu^+ stabilization *via* a single-atom modifier for CO_2 electroreduction. J Mater Chem A, 2020, 8: 25970–25977
19 Daiyan R, Lovell EC, Huang B, *et al.* Uncovering atomic-scale stability and reactivity in engineered zinc oxide electrocatalysts for controllable syngas production. Adv Energy Mater, 2020, 10: 2001381
20 He Q, Liu D, Lee JH, *et al.* Electrochemical conversion of CO_2 to syngas with controllable CO/H_2 ratios over Co and Ni single-atom catalysts. Angew Chem Int Ed, 2020, 59: 3033–3037
21 Ye L, Ying Y, Sun D, *et al.* Highly efficient porous carbon electrocatalyst with controllable N-species content for selective CO_2 reduction. Angew Chem Int Ed, 2020, 59: 3244–3251
22 Zheng X, De Luna P, García de Arquer FP, *et al.* Sulfur-modulated tin sites enable highly selective electrochemical reduction of CO_2 to formate. Joule, 2017, 1: 794–805
23 Tomisaki M, Kasahara S, Natsui K, *et al.* Switchable product selectivity in the electrochemical reduction of carbon dioxide using boron-doped diamond electrodes. J Am Chem Soc, 2019, 141: 7414–7420
24 Tang C, Zhang R, Lu W, *et al.* Fe-doped CoP nanoarray: A monolithic multifunctional catalyst for highly efficient hydrogen generation. Adv Mater, 2017, 29: 1602441
25 Yu XY, Feng Y, Jeon Y, *et al.* Formation of Ni-Co-MoS_2 nanoboxes with enhanced electrocatalytic activity for hydrogen evolution. Adv Mater, 2016, 28: 9006–9011
26 Yang M, Jiao L, Dong H, *et al.* Conversion of bimetallic MOF to Ru-doped Cu electrocatalysts for efficient hydrogen evolution in

alkaline media. Sci Bull, 2021, 66: 257–264
27 Yao N, Li P, Zhou Z, *et al.* Synergistically tuning water and hydrogen binding abilities over Co_4N by Cr doping for exceptional alkaline hydrogen evolution electrocatalysis. Adv Energy Mater, 2019, 9: 1902449
28 Ito Y, Shen Y, Hojo D, *et al.* Correlation between chemical dopants and topological defects in catalytically active nanoporous graphene. Adv Mater, 2016, 28: 10644–10651
29 Deng S, Zhong Y, Zeng Y, *et al.* Directional construction of vertical nitrogen-doped 1T-2H $MoSe_2$/graphene shell/core nanoflake arrays for efficient hydrogen evolution reaction. Adv Mater, 2017, 29: 1700748
30 Zhang A, He R, Li H, *et al.* Nickel doping in atomically thin tin disulfide nanosheets enables highly efficient CO_2 reduction. Angew Chem Int Ed, 2018, 57: 10954–10958
31 Geng Z, Kong X, Chen W, *et al.* Oxygen vacancies in ZnO nanosheets enhance CO_2 electrochemical reduction to CO. Angew Chem Int Ed, 2018, 57: 6054–6059
32 Liu L, Jiang Y, Zhao H, *et al.* Engineering coexposed {001} and {101} facets in oxygen-deficient TiO_2 nanocrystals for enhanced CO_2 photoreduction under visible light. ACS Catal, 2016, 6: 1097–1108
33 Yuan T, Hu Z, Zhao Y, *et al.* Two-dimensional amorphous SnO_x from liquid metal: Mass production, phase transfer, and electrocatalytic CO_2 reduction toward formic acid. Nano Lett, 2020, 20: 2916–2922
34 Zheng T, Jiang K, Ta N, *et al.* Large-scale and highly selective CO_2 electrocatalytic reduction on nickel single-atom catalyst. Joule, 2019, 3: 265–278
35 Chen M, Gao L. Synthesis and characterization of cadmium selenide nanorods *via* surfactant-assisted hydrothermal method. J Am Ceramic Soc, 2005, 88: 1643–1646
36 Chen CC, Chao CY, Lang ZH. Simple solution-phase synthesis of soluble CdS and CdSe nanorods. Chem Mater, 2000, 12: 1516–1518
37 Zhang Q, Gupta S, Emrick T, *et al.* Surface-functionalized CdSe nanorods for assembly in diblock copolymer templates. J Am Chem Soc, 2006, 128: 3898–3899
38 Vinson J, Rehr JJ. *Ab initio* Bethe-Salpeter calculations of the X-ray absorption spectra of transition metals at the L-shell edges. Phys Rev B, 2012, 86: 195135
39 Mohanty B, Jena BK, Kandasamy M, *et al.* The role of Se vacancies and Fe doping of nickel selenide in the water oxidation reaction. Sustain Energy Fuels, 2020, 4: 3058–3065
40 Wu Y, Zhai P, Cao S, *et al.* Beyond d orbits: Steering the selectivity of electrochemical CO_2 reduction *via* hybridized sp band of sulfur-incorporated porous Cd architectures with dual collaborative sites. Adv Energy Mater, 2020, 10: 2002499
41 Gao FY, Hu SJ, Zhang XL, *et al.* High-curvature transition-metal chalcogenide nanostructures with a pronounced proximity effect enable fast and selective CO_2 electroreduction. Angew Chem Int Ed, 2020, 59: 8706–8712
42 Wang C, Cao M, Jiang X, *et al.* A catalyst based on copper-cadmium bimetal for electrochemical reduction of CO_2 to CO with high Faradaic efficiency. Electrochim Acta, 2018, 271: 544–550
43 Zeng L, Shi J, Luo J, *et al.* Silver sulfide anchored on reduced graphene oxide as a high-performance catalyst for CO_2 electroreduction. J Power Sources, 2018, 398: 83–90
44 Li H, Wen P, Itanze DS, *et al.* Colloidal silver diphosphide (AgP_2) nanocrystals as low overpotential catalysts for CO_2 reduction to tunable syngas. Nat Commun, 2019, 10: 5724
45 Xu J, Li X, Liu W, *et al.* Carbon dioxide electroreduction into syngas boosted by a partially delocalized charge in molybdenum sulfide selenide alloy monolayers. Angew Chem Int Ed, 2017, 56: 9121–9125
46 Zhang Z, Ahmad F, Zhao W, *et al.* Enhanced electrocatalytic reduction of CO_2 *via* chemical coupling between indium oxide and reduced graphene oxide. Nano Lett, 2019, 19: 4029–4034
47 Zhang S, Kang P, Meyer TJ. Nanostructured tin catalysts for selective electrochemical reduction of carbon dioxide to formate. J Am Chem Soc, 2014, 136: 1734–1737
48 Yao T, Liu L, Xiao C, *et al.* Ultrathin nanosheets of half-metallic monoclinic vanadium dioxide with a thermally induced phase transition. Angew Chem Int Ed, 2013, 52: 7554–7558
49 Zhang W, Hu Y, Ma L, *et al.* Progress and perspective of electrocatalytic CO_2 reduction for renewable carbonaceous fuels and chemicals. Adv Sci, 2018, 5: 1700275
50 Singh MR, Goodpaster JD, Weber AZ, *et al.* Mechanistic insights into electrochemical reduction of CO_2 over Ag using density functional theory and transport models. Proc Natl Acad Sci USA, 2017, 114: E8812–E8821

Acknowledgements This work was supported by the National Natural Science Foundation of China (12025505 and 21873050), China Ministry of Science and Technology (2017YFA0208300), the Open Fund Project of State Key Laboratory of Environmentally Friendly Energy Materials (20KFHG08), and the Youth Innovation Promotion Association CAS (CX2310007007 and CX2310000091). We thank National Synchrotron Radiation Laboratory (NSRL), Beijing Synchrotron Radiation Facility (BSRF), Shanghai Synchrotron Radiation Facility (SSRF) for the synchrotron beam time.

Author contributions Yao T, Chen T and Zhu W developed the idea and designed the experiments. Chen T, Shen X, Zhang W, Wang L and Ding T performed the catalyst synthesis and characterizations, FT-IR measurements and electrochemical experiments. Cao L and Ding T performed the TEM characterization. Zhang W and Liu X carried out the XAFS calculation and analysis on Cd, Se, and Ag K-edge. Chen T and Yao T co-wrote the paper. Liu T and Li Y performed the DFT calculations. All authors discussed the results and commented on the manuscript.

Conflict of interest The authors declare that they have no conflict of interest.

Supplementary information Experimental details and supporting data are available in the online version of this paper.

Tao Chen received his BSc (2016) and MSc (2019) degrees at the School of National Defense Science and Technology, Southwest University of Science and Technology, China. He is currently a PhD student at the National Synchrotron Radiation Laboratory, University of Science and Technology of China. His present research interest focuses on the design of 2D catalysts and their application in photoelectrocatalysis.

Tao Yao received his PhD degree from the National Synchrotron Radiation Laboratory, University of Science and Technology of China in 2011. He is currently a professor of the University of Science and Technology of China and principle investigator (PI) of the group of "Synchrotron Radiation and Energy Material". His scientific interest foucses on *operando*/time-resolved spectroscopy and the development of new catalysts for energy conversion.

协同电子调控增强类金属特性CdSe纳米棒的电催化CO_2还原性能

陈涛[1,2], 刘天阳[3], 沈心怡[1], 张伟[1], 丁韬[1], 王兰[1,2], 刘潇康[1], 曹林林[1], 竹文坤[2*], 李亚飞[3*], 姚涛[1*]

摘要 通过定制催化剂的电子特性以达到合适的中间体吸附能, 从而获得高选择性, 是一种可用于设计先进的CO_2电还原催化剂的有前景的策略, 在本文中, 我们报道了一种通过协同调控CdSe纳米棒的电子结构以促进电化学CO_2还原的方法. 银掺杂与硒空位协同调控了CdSe纳米棒的电子结构, 导致该结构显示出类金属特性, 从而加速了CO_2电还原过程中的电子传递. 此外, 原位同步辐射傅里叶变换红外光谱和理论计算表明, 银掺杂和硒空位的耦合加速了CO_2活化过程, 同时降低了将CO_2转化为*COOH中间体的能垒, 从而有效增强了电催化CO_2还原性能. 与原始的CdSe纳米棒相比, 银掺杂的CdSe纳米棒表现出2.7倍的电流密度和1.9倍的法拉第效率.

